Quantifying angular dependence of spin-orbit torques in Ta/CoFeB/MgO trilayers with perpendicular magnetic anisotropy

Yunpeng Chen, Halise Celik, Tao Wang, Harsha Kannan, Ilya N. Krivorotov, and John Q. Xiao

Phys. Rev. B **95**, 144405 — Published 7 April 2017

DOI: 10.1103/PhysRevB.95.144405

Quantifying angular dependence of spin-orbit torques in Ta/CoFeB/MgO trilayers with perpendicular magnetic anisotropy

Yunpeng Chen[1], Halise Celik[1], Tao Wang[1], Harsha Kannan[1], Ilya N. Krivorotov[2], and John Q. Xiao[1]

[1]*Department of Physics and Astronomy, University of Delaware, Newark, DE 19716, USA*
[2]*Deparment of Physics and Astronomy, University of California, Irvine, CA 92697, USA*

The spin-orbit interactions in heavy-metal/ferromagnet heterostructures have attracted considerable attention because they provide an efficient way to manipulate the magnetization with strong current-driven spin-orbit torques (SOTs) via the spin Hall effect in the heavy metal or Rashba effect due to the symmetry breaking at the interface. Theoretical calculations predict no dependence of the SOTs on the out-of-plane angle of magnetization due to spin Hall effect, but Rashba effect induces a non-trivial angular dependence of SOTs. Quantitative measurements with adiabatic harmonic Hall technique have observed the angular dependence in Ta/CoFeB/MgO or Pt/Co/AlO_x with perpendicular magnetic anisotropy. However, this method is complicated because the signal consists of both anomalous and planar Hall contributions. In addition, the fitting of the measurement data is sensitive to the fitting parameters, particularly to the perpendicular anisotropy, in certain angle region (40-70 degree). To avoid this uncertainty, we have developed a scheme to quantify the angular dependence of SOTs based on the magneto-optic Kerr effect (MOKE) with field calibration. Without fitting procedures, we precisely determine the SOTs and their angle dependence on the magnetization orientation. We observe a strong angular dependence that is different from the previous experimental observations. Based on this strong dependence, we conclude that a Rashba effect at the same interface, that is responsible for the perpendicular magnetic anisotropy, is the dominant mechanism for the current-driven SOTs in this system.

I. INTRODUCTION

In-plane current in heavy metal (HM)/ ferromagnet (FM)/metal-oxide (MO_x) trilays generates spin-orbit torques (SOTs) that enable a new efficient method to control the magnetization of FM layer. The spin-orbit driven magnetic dynamics such as magnetic reversal [1-6], high-frequency oscillation [7-11], domain-wall motion [12-14] and skyrmion manipulation [15, 16] have been demonstrated and may find critical applications in novel magnetic memory and logic devices. In a typical structure depicted in Fig. 1, the charge current along the *x*-direction generates damping-like torque of $\vec{M}\times(\vec{M}\times\hat{y})$ [17] and field-like torque $\vec{M}\times\hat{y}$ [18] on the FM layer. The damping-like torque is also referred to Slonczewski-like torque or spin-transfer torque that describes the transfer of angular momentum from spin-polarized current to the local magnetization. The field-like term was missed in the early spin-transfer torque measurements since the spin dephasing length is shorter than the FM layer in the structures [19, 20]. The modified Landau-Lifshitz-Gilbert (LLG) equation is usually used to study the magnetic dynamics induced by SOTs as [21, 22]

$$\frac{d\vec{M}}{dt}=-\gamma\vec{M}\times\vec{H}+\frac{\alpha}{M_s}\vec{M}\times\frac{d\vec{M}}{dt}+a\vec{M}\times\vec{\sigma}+b\vec{M}\times(\vec{\sigma}\times\vec{M}) \quad (1)$$

where the third and fourth terms on the right-hand side correspond to the field-like torque and damping-like torque, respectively, with related magnitude *a* and *b*, $\vec{\sigma}$ is a unit vector for the spin direction in spin-polarized current or spin accumulation at the HM/FM interface. The effective fields corresponding to the field-like and damping-like torque can be defined as $\vec{H}_f=-a\vec{\sigma}/\gamma$ and $\vec{H}_t=-b\vec{\sigma}\times\vec{M}/\gamma$, respectively. Because $\vec{H}_f$ and $\vec{H}_t$ have different dependence on magnetization vector $\vec{M}$, one can separately detect them in designed experiment configurations.

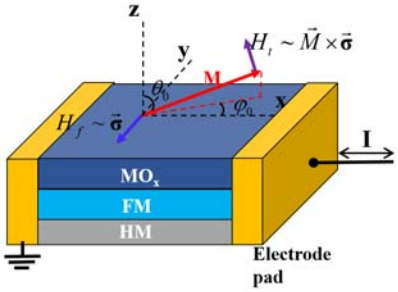

FIG.1. Schematics of SOTs in a trilayer system.

Two mechanisms have been proposed to explain the generation of spin-orbit torques: the spin Hall effect [1, 4, 8, 23-27] (SHE) in the bulk materials with strong spin-

orbit interaction and the Rashba-Edelstein effects [14, 18, 27-30] due to the interfacial spin-orbit coupling. Much effort has been dedicated to identify the dominant mechanism of the SOTs, because, phenomenologically, both SHE and Rashba effect cause the torques with the same expressions. Although it has been pointed out that the damping-like and field-like torques are dominated by SHE and Rashba effect, respectively [31-33], each torque contains the contributions from both SHE and Rashba effect [18, 27, 34, 35]. The SOTs in HM/FM bilayers with in-plane magnetic anisotropy have been extensively investigated. The damping-like torque is usually found to be larger than the field-like torque [1, 24, 26, 36], indicating the SHE is strong in the bilayers with in-plane anisotropy. Xin et al. [36] identified the contributions of the SHE and Rashba effect to SOTs in Pt/CoFeB bilayers by inserting a copper layer to minimize the Rashba effect. However, the same scheme cannot be applied to Ta/CoFeB/MgO trilayers with perpendicular magnetic anisotropy (PMA) since it will dramatically affect the PMA [39-42]. Different from the in-plane bilayers, the Ta/CoFeB/MgO trilayers with PMA show strong Rashba effect (field-like torque), owing to the interfacial symmetry breaking and hybridization of electronic states at Ta/CoFeB and CoFeB/MgO interfaces [43, 44]. The ratio between field-like and damping-like torques are detected to be two [43], three [44], six [45, 46], and up to eight (this study), which is significantly affected by the modification of the interfaces through thermal annealing [47]. The Rashba induced SOTs are closely related with the PMA [47], while the mechanism needs further theoretical investigations.

The theoretical models based on the Boltzmann equation and drift-diffusion equations suggest the two mechanisms with different dependence on the thickness of HM layer [34, 35]. Allen et al. [48] measured the SOTs in β-Ta/CoFeB bilayers as a function of Ta thickness with STT-FMR technique. The results deviate from the theoretical predictions at the ultrathin-film region. The sign change of the field-like torque at the small thickness of Ta (<1.5 nm) is hard to explain. The Ta-thickness dependent studies in Ta/CoFeB/MgO trilayer with PMA were performed through harmonic Hall measurements [43, 44]. Zhang et al. [43] attribute the SOTs to the SHE in Ta layer. However, the field-like torque is 2 times of the damping-like torque, which does not support the SHE induced SOTs. If Rashba effect dominates, then the saturation rate of the field-like torque with the increase of Ta thickness is too small comparing to the theoretical predictions. Kim et al [44] also observed non-trivial thickness dependence of SOTs at ultrathin region (<0.5 nm). The issue of the thickness dependent study is that the behavior of SOT could be originated from the thickness modified film conductivity or the interface properties. The analysis of the thickness effect requires more careful treatments. Other effects such as the reflection of spin current at FM/MO_x interface could contribute to the SOTs [47]. The origin of the current-induced spin-orbit torques in Ta/CoFeB/MgO with PMA remains to be elusive.

One promising method to distinguish between SHE and Rashba-driven SOTs is through the dependence of spin-orbit torques on the angular direction of the magnetization. Theories based on the bulk SHE combined with Boltzmann transport equation [27] suggest both field-like and damping-like torques are independent on the rotation of magnetization normal to the film plane. On the other hand, a model with the Rashba spin-orbit coupling with comparable strength to the exchange coupling [50] predicts a strong angular dependence in spin-orbit torques. In addition, the angular dependence of SOTs has a critical impact on the magnetic dynamics and hence is important to understand for optimizing the spin-orbit spintronics devices. In this paper, we report the quantification of the angular dependence of SOTs in Ta (2 nm)/CoFeB (1 nm)/ MgO (3 nm) trilayers. The angular dependence of SOTs is determined from two techniques: adiabatic harmonic Hall and MOKE. We show that the harmonic Hall technique employed in the previous studies [43-47, 51] is inaccurate in determining the angular dependence of SOTs, particularly in the medium polar angle region ($\theta = 40° - 70°$), because the fitting of the measurement curves is very sensitive to the fitting parameters like perpendicular anisotropy. In MOKE measurements, we implement a field-calibration method to quantify the SOTs accurately at various polar angles of magnetization. The obtained non-trivial angular dependence of SOTs is distinct from the previous experimental observations. The results suggest that the Rashba effect is the dominant contribution to SOTs in Ta/CoFeB/MgO structures.

The rest of this paper is organized as follows. In Section II, we describe the sample structure, fabrication and the optimization of PMA in Ta/CoFeB/MgO trilayers. In Section III, we discuss the reorientation of magnetization due to the effective spin-orbit fields. In two measurement geometries, the modulation of the polar or azimuthal angle of the magnetization is only caused by either $\vec{H}_t$ or $\vec{H}_f$, based on which we quantify them independently. In Section IV, we report the measurements of $\vec{H}_t$ and $\vec{H}_f$ using harmonic Hall technique. The angular dependence of SOTs is obtained by fitting the measurement curves with analytical formula. We show the fitting results vary significantly with the effective perpendicular anisotropy field that is difficult to be precisely determined. In Section V, we implement a field calibration in the MOKE technique, leading to the accurate measurement of $\vec{H}_t$ and $\vec{H}_f$. In addition, we developed an algorithm to determine the SOTs at different

polar angles of magnetization. Both the magnitude and angular dependence of SOTs indicate the Rashba effect is much stronger than SHE in Ta/CoFe/MgO system. The summary and conclusions are presented in Section VI.

II. Ta/CoFeB/MgO trilayers with PMA

A. Sample fabrication

The trilayer samples composed of Ta/$Co_{40}Fe_{40}B_{20}$/MgO were grown on a thermally oxidized Si wafer by magnetron sputtering. The base pressure of the vacuum chamber is 3×10^{-8} torr, and the H_2O partial pressure is 3×10^{-9} Torr. Ta and CoFeB layer were deposited by dc sputtering at a rate of 1 Å/s. MgO was deposited from a MgO target by RF sputtering at a rate of 0.04 Å/s. The argon pressures during the deposition were 3 mTorr for Ta and CoFeB deposition and 1.1 mTorr during MgO deposition. Then a 7-nm SiO2 was grown as the capping layer to protect the MgO layer from degradation during the following annealing and fabrication process. For the harmonic Hall voltage measurements, the thin films were lithographically patterned into Hall bars with 500 μm wide and 3mm long. The samples used for MOKE measurements were patterned into 30 μm × 30 μm squares. The contact pads consist of Ta (5)/Cu (200)/Au (50) (the numbers in parentheses are thicknesses in nanometers).

B. Dependence of PMA on the film thickness

The interfacial PMA in Ta/CoFeB/MgO trilayers arises from the hybridization between the ferromagnetic atoms (Co and Fe) and the oxygen atoms in MgO [41]. A more recent study suggests that the bottom metallic layer like Ta also significantly influences the perpendicular anisotropy [42]. Moreover, the annealing treatments are necessary for the development of PMA and tunneling magnetoresistance (TMR) in the perpendicular magnetic tunnel junction. With rapid thermal annealing technique. Wang et al. [40] have achieved over 100% TMR. Here, we adopted the similar thermal treatment at 340°C for 3 min. We investigated the influence of the thickness of an individual layer on the development of PMA. Three sets of samples were fabricated. Each group of the sample has the structure with thickness variation in one of the three layers. The structures are Ta (x)/CoFeB (1.2)/MgO (3), Ta (2)/CoFeB (y)/MgO (3), and Ta (2)/CoFeB (1.2)/ MgO (z). The PMA of each sample is investigated via anomalous Hall effect (AHE) measurement, where the Hall voltage is detected as sweeping the magnetic field in the direction normal to the film plane. As shown in Fig. 2, the square-shaped hysteresis loop indicates good PMA. Summarizing all results, we obtain the required thickness ranges for PMA, which are $t_{Ta} > 1$ nm, 1.5 nm > $t_{CoFeB} >$ 0.8 nm, and $t_{MgO} > 1.1$ nm. We, therefore, choose the structure of Ta (2)/ CoFeB (1)/ MgO (3) to measure SOTs.

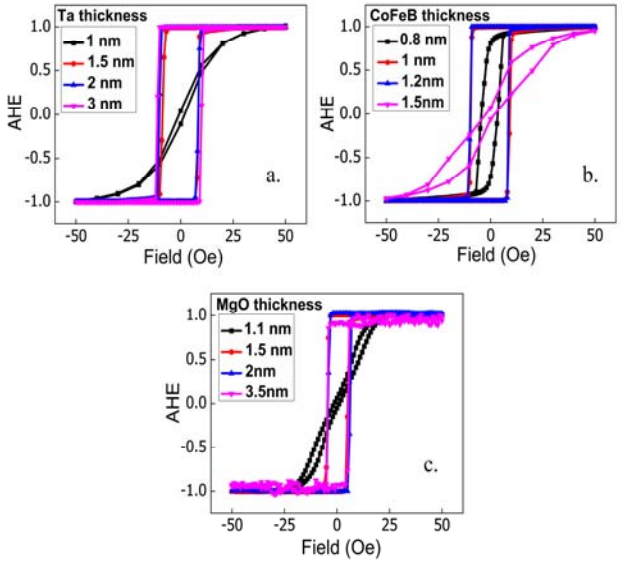

FIG.2. The AHE hysteresis loops of three groups of sample: (a) Ta (x)/CoFeB (1.2)/MgO (3), (b) Ta (2)/CoFeB (y)/MgO (3), and (c) Ta (2)/CoFeB (1.2)/ MgO (z).

III. Manipulation of magnetization angle due to spin-orbit torques

The SOTs rotate the magnetization from its equilibrium orientation. As shown in Fig. 1, θ_0 and φ_0 are the polar and azimuthal angle of the magnetization in FM layer at equilibrium direction. We also define the polar and azimuthal angle of the magnetic field as θ_H and φ_H. The in-plane current generates effective fields $\Delta H_{x,y,z}$ of SOTs, leading to the modulation of the magnetization angle ($\Delta\theta$ and $\Delta\varphi$). To determine the current-induced SOTs, we derive the relation between SOTs and the change of magnetization angle.

The magnetic energy of the system can be written as

$$E = -K_p \cos^2\theta - K_I \sin^2\varphi \sin^2\theta - \vec{M}\cdot\vec{H} \qquad (2)$$

where K_p is the effective out-of-plane anisotropy energy including demagnetizing energy and perpendicular surface anisotropy $K_\perp$, and K_I is the in-plane uniaxial anisotropy energy. In a magnetic thin film, K_p can be expressed as $K_p = K_\perp - \frac{1}{2}M_s^2$. The corresponding effective out-of-plane and in-plane anisotropy fields are $H_p = \frac{2K_p}{M_s}$ and $H_I = \frac{2K_I}{M_s}$. To find the equilibrium

magnetization directions (θ_0 and φ_0), one can solve the equations

$$\left.\frac{\partial E}{\partial \theta}\right|_{\theta=\theta_0,\varphi=\varphi_0} = 0 \tag{3}$$

$$\left.\frac{\partial E}{\partial \varphi}\right|_{\theta=\theta_0,\varphi=\varphi_0} = 0 \tag{4}$$

The small perturbations ($\Delta\theta$ and $\Delta\varphi$) to the magnetization direction are given by

$$\Delta\theta = \frac{\partial\theta}{\partial H_x}\Delta H_x + \frac{\partial\theta}{\partial H_y}\Delta H_y + \frac{\partial\theta}{\partial H_z}\Delta H_z \tag{5}$$

$$\Delta\varphi = \frac{\partial\varphi}{\partial H_x}\Delta H_x + \frac{\partial\varphi}{\partial H_y}\Delta H_y + \frac{\partial\varphi}{\partial H_z}\Delta H_z \tag{6}$$

We assume that the external magnetic field is much larger than the in-plane uniaxial anisotropy, so that $\varphi_0 = \varphi_H$. We further assume the direction of the external magnetic field is along either *x* or *y*-axis. Eqs. (5) and (6) under small angle approximation can be expressed as [51]

$$\Delta\theta = \frac{\cos\theta_0(\Delta H_x\cos\varphi_H + \Delta H_y\sin\varphi_H) - \sin\theta_0\Delta H_z}{(H_P - H_I\sin^2\varphi_H)\cos 2\theta_0 + H\cos(\theta_H - \theta_0)} \tag{7}$$

$$\Delta\varphi = \frac{-\Delta H_x\sin\varphi_H + \Delta H_y\cos\varphi_H}{-H_I\sin\theta_0\cos 2\varphi_H + H\sin\theta_H} \tag{8}$$

Eqs. (7) and (8) can be further simplified in the particular field and magnetic anisotropy configurations. Below, we discuss two scenarios that will be used in the measurements. The damping-like SOT field $\vec{H}_t = -b\vec{\sigma}\times\vec{M}/\gamma$ is always normal to the magnetization and the field-like SOT field $\vec{H}_f = -a\vec{\sigma}/\gamma$ does not depend on the magnetization. One can separate the damping-like and field-like SOTs based on their symmetries with respect to the magnetization. As illustrated in Fig. 3a, we apply both the external magnetic field and in-plane current along the *x*-axis, leading to spin polarization $\vec{\sigma}$ in the *y* direction. We call this set up as the $H /\!/ I$ configuration. The damping-like torque causes the modulation of polar angle of magnetization and the field-like torque changes the azimuthal angle of magnetization. In addition to the SOT effective fields, the current generates Oersted field exerting on the FM layer as H_{Oe} along the *y* direction. One can write the current-induced effective fields as $\Delta H_x = -H_t\cos\theta_0$, $\Delta H_y = H_f + H_{Oe}$ and $\Delta H_z = H_t\sin\theta_0$. Then from Eqs. (7) and (8), we obtain the modulation of the magnetization angle as

$$\Delta\theta = -\frac{H_t}{H_P\cos 2\theta_0 + H\sin\theta_0} \tag{9}$$

$$\Delta\varphi = \frac{1}{H - H_I\sin\theta_0}\left(H_f + H_{Oe}\right) \tag{10}$$

It is, therefore, obvious that damping-like torque/field-like torque changes the polar/azimuthal angle of the magnetization.

In the second geometry (the $H \perp I$ configuration) depicted in Fig. 3b, we apply the magnetic field along the *y*-axis so that the magnetization rotates in the *y*-*z* plane. The in-plane current along the *x*-axis creates the same spin polarization $\vec{\sigma}$ as the previous configuration. Therefore, the *y*-component of current induced effective field is the same as $\Delta H_y = H_f + H_{Oe}$. And the effective field due to the damping-like torque is in the *x*-direction as $\Delta H_x = -H_t$. From Eqs. (7) and (8), we get the expressions of magnetization change

$$\Delta\theta = \frac{\left(H_f + H_{Oe}\right)\cos\theta_0}{(H_P - H_I)\cos 2\theta_0 + H\sin\theta_0} \tag{11}$$

$$\Delta\varphi = \frac{1}{H + H_I\sin\theta_0}H_t \tag{12}$$

In this scenario, the modulation of polar angle $\Delta\theta$ is proportional to the field-like torque and Oersted field, and the modulation of the azimuthal angle $\Delta\varphi$ depends on the damping-like torque.

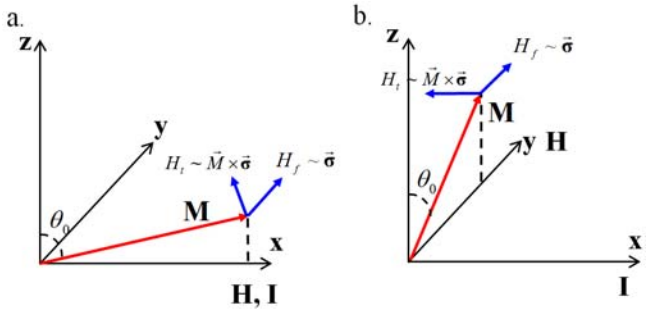

FIG.3. The sketches of SOTs measurement in two configurations: (a) $H /\!/ I$ configuration and (b) $H \perp I$ configuration.

The effective fields of SOTs alter the magnetization angle, resulting in a change of the Hall signal. The Hall voltage consists of the anomalous Hall (AHE) and planar Hall (PHE) contributions. The detected single was mostly attributed to AHE because AHE response is usually much larger than PHE in typical ferromagnetic metals and their alloys [2, 44 45]. Kim et al. [49] only considered the AHE component of the Hall voltage and derived a simple algorithm for extracting the magnitude of SOTs in Ta/CoFeB/MgO. Later, the PHE correction was implemented into the model by Garello et al. [45] to improve the method. However, the procedure to determine the SOTs from measurement data becomes complicated. Here, we performed the same measurements in Ref [44-47].

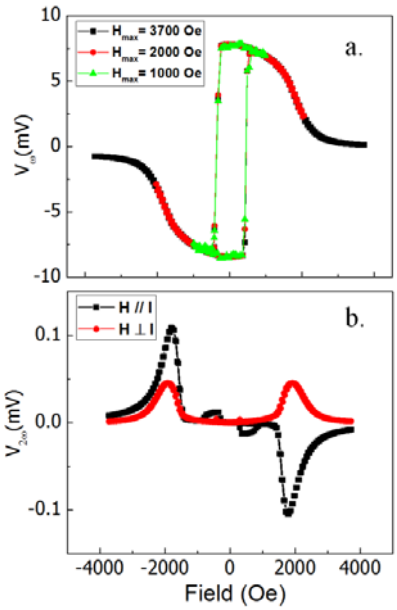

FIG.4. (a) First harmonic loops under different applied fields; (b) Second harmonic loops under $H // I$ and $H \perp I$ geometries.

A sinusoidal AC current I_{ac} with the frequency of 323.4 Hz is applied to the Hall bar along the *x*-axis. The amplitude of I_{ac} is 5.7 mA. The resistivity of CoFeB and Ta thin film at 1 nm are 246 μΩ·cm and 256 μΩ·cm, respectively. Assuming the bilayer as a parallel circuit, the electric current density in Ta is 0.38 $\times 10^6$ A·cm^{-2}. The current causes small oscillations of the magnetization through SOTs and Oersted field, leading to the first and second order harmonic Hall voltages detected by a lock-in amplifier. The DC AHE signal is related to the polar angle of magnetization as $V_A = \frac{1}{2}\Delta R_A I \cos\theta$ and the DC PHE signal is given by $V_P = \frac{1}{2}\Delta R_P I \sin^2\theta \sin 2\varphi$. When azimuthal angle φ_0 is 0° or 90°, the expressions of the harmonic Hall voltages are

$$V_\omega = \frac{1}{2}\Delta R_A I_{ac,FM} \cos\theta_0 \tag{13}$$

$$V_{2\omega} = \frac{1}{2} I_{ac,FM} \sin\theta_0 \left(\Delta R_A \Delta\theta \pm \frac{1}{2}\Delta R_P \sin\theta_0 \Delta\varphi \right) \tag{14}$$

where the anomalous Hall resistance ΔR_A is 8.20 Ohm and the planar Hall resistance ΔR_P is 0.32 Ohm for 1 nm CoFeB thin film, $I_{ac,FM}$ is the AC current in FM layer that is equal to 1.9 mA, the sign in Eq. (14) is negative when $\varphi_0 = 0°$ and positive when $\varphi_0 = 90°$. The AHE voltage dominates the Hall signal.

In order to separately determine H_t and H_f, we performed the Hall measurements in the two configurations in Fig. 3. The magnetic field is applied in the film plane with a small tilting angle ($\theta_H = 85°$) to avoid the formation of domain walls. We plot the first and second order Harmonic response as a function of the external field in Fig. 4a and 4b. The magnetic switching doesn't vary with the different applied field, indicating the single domain state. It is important to note that the domain structures could be created at high polar angles. The sub-100nm structures will be preferred to validate the single-domain assumption. In the $H // I$ configuration (Fig. 3a), the modulation of polar angle $\Delta\theta$ is proportional to H_t, expressed in Eq. (9). Therefore, the second harmonic signal is mostly attributed to damping-like torque. The first-order Hall voltage reduces with the increase of magnetic field. The equilibrium polar angle θ_0 of magnetization at each magnetic field is obtained from the first harmonic Hall response by Eq (13). From Eqs. (9) and (14), we obtain the expression of second harmonic voltage as

$$V_{2\omega} = -\frac{1}{4}\Delta R_A I_{ac,FM} \frac{\sin\theta_0 H_t}{H_P \cos 2\theta_0 + H \sin\theta_0} - \frac{1}{2}\Delta R_P I_{ac,FM} \frac{\sin^2\theta_0 \left(H_f + H_{Oe}\right)}{H - H_I \sin\theta_0} \tag{15}$$

Fig. 5a shows the fitting of the second harmonic data from Eq. (15) with parameters of $H_t = 1.2$ Oe, $H_f = 2.9$ Oe, $H_P = 2070$ Oe, and $H_I = 50$ Oe. Here, the effective perpendicular field H_P is determined as the magnetic field at which the magnetization saturates along the film plane, in the first-order harmonic loop in Fig. 4a.

Similarly, in the $H \perp I$ configuration (Fig. 3b), we derive the second harmonic response expressed as

$$V_{2\omega} = \frac{1}{4}\Delta R_A I_{ac,FM} \frac{\sin\theta_0 \cos\theta_0 \left(H_f + H_{Oe}\right)}{H_P \cos 2\theta_0 + H \sin\theta_0} + \frac{1}{2}\Delta R_P I_{ac,FM} \frac{\sin^2\theta_0 H_t}{H + H_I \sin\theta_0} \tag{16}$$

The AHE voltage is dominated by field-like torque. We fit the second harmonic curve in Fig. 5b using Eq. (16) with the same parameters as in Fig. 5a. We neglect the current-induced Oersted field in both situations because it is much smaller than the SOT fields. The in-plane Oersted field is calculated from Ampere's Law as $H_{Oe} = \frac{I}{2w} = 0.04$ Oe, where $w = 500$ μm is the width of the Hall bar and current in Ta is $I = 3.8$ mA. We then calculate the coefficients of

SOTs as $\frac{H_t}{j_{Ta}} = 3.16$ Oe/ 10^6 A cm^{-2} and $\frac{H_f}{j_{Ta}} = 7.63$ Oe/ 10^6 A cm^{-2}. Assuming H_t is only caused by SHE, we calculate the spin Hall angle at the perpendicular state as $\theta_{SH} = \frac{2eM_s tH_t}{\hbar \cdot j_{Ta}} = 0.09$, where e is the electron charge, M_s = 10^6 A/m is the saturation magnetization of CoFeB, and the thickness of CoFeB t is 1 nm.

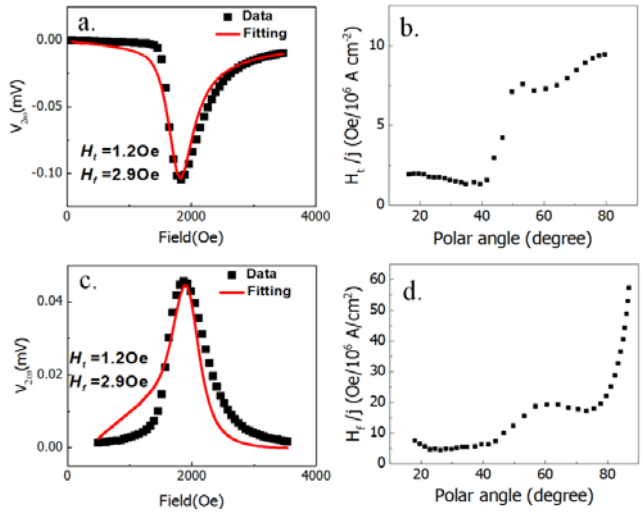

FIG.5. The fitting of second harmonic curves under (a) $H \,//\, I$ and (c) $H \perp I$ geometries. The fitted values of H_t and H_f are 1.2 Oe and 2.9 Oe, respectively. (b) and (d) present the coefficient of damping-like torque (H_t / j_{Ta}) and field-like (H_f / j_{Ta}) torque as a function of the polar angle of $\vec{M}$.

The magnitude of spin Hall angle at θ=0 is consistent with the previous reports on Ta/CoFeB/MgO [43-47] and in-plane structures [1,8,9].We extract the angular dependence by fitting the second harmonic Hall data. The damping-like torque is increasing with the polar angle and becomes the maximum when the magnetization is in the film plane due to the angular dependence of Rashba induced SOTs. The constant values of H_t and H_f have been used in the fitting, i.e. no dependence on the magnetization direction. The deviations between experimental and fitting curves in Fig. 5a and 5c indicate the angular dependence of H_t and H_f [42]. By solving Eqs. (15) and (16) with known values of $V_{2\omega}$, ΔR_A , ΔR_P , $I_{ac,FM}$, θ_0 , H_P , and H_I , we calculate the effective fields due to SOTs at each polar angle θ_0 . It is important to note that the dependence of H_t and H_f on the azimuthal angle φ_0 is neglected, which might cause some additional errors [45]. As shown in Fig. 5b and 5d, both H_t and H_f increase with the polar angle and reach the maximum magnitude when the magnetization is in the film plane.

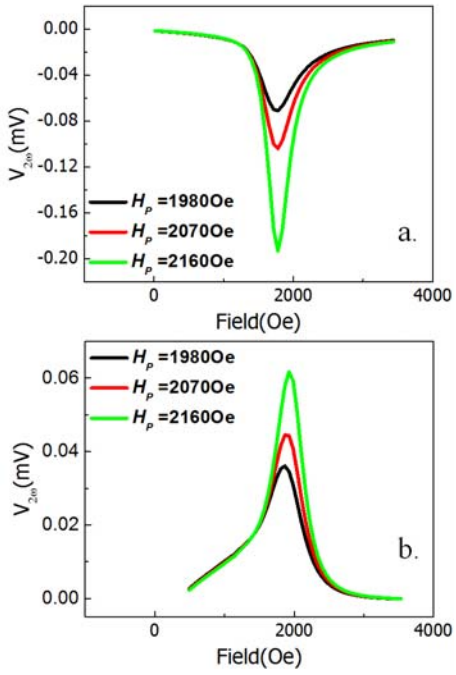

FIG.6. The fitting curves of second harmonic voltage with different values of perpendicular anisotropy field H_P in (a) the $H \,//\, I$ and (b) the $H \perp I$ configurations.

The profile of the SOTs in between 40 and 70 degree is owing to the uncertainty of the calculation. The fitting curves do not vary much corresponding to different effective anisotropy fields H_P in the low and high field region, shown in Fig. 6, suggesting the accuracy of the harmonic Hall measurements. However, the fitting results are sensitive to the effective anisotropy field near the peak, where the polar angle of magnetization is between 40 and 70 degree. A small uncertainty in the value of H_P leads to a significant error in the calculation. As shown in Fig. 6, a less than 5% change (90 Oe) in H_P leads to a massive variation of the fitting curves in both configurations. In conclusion, the harmonic Hall technique may not be an accurate method to study the angular dependence of SOTs. In the next part, we will demonstrate a proper measurement scheme with MOKE technique and field calibration.

IV. Detection of spin-orbit torques with MOKE

The MOKE response originates from the interaction between light polarization and magnetization. With normal light incidence, the rotation of the light

polarization angle due to a magnetic surface can be expressed as

$$\Psi = \alpha_{polar} m_z + \beta_{quadratic} m_x m_y \quad (17)$$

where α_{polar} and $\beta_{quadratic}$ denote the coefficient for the polar and quadratic MOKE signals, respectively. The first (polar MOKE) and the second term (quadratic MOKE) on the right-hand side of Eq. (17) are analogous to the forms of AHE and PHE respectively. The MOKE technique has an advantage over the electric Hall measurements in distinguishing the polar and quadratic MOKE response by the polarization of the light. When the incident light is 45° linearly polarized with respect to the *x*-axis, the MOKE signal only has polar contribution [36, 52]. The configuration of our MOKE measurements is depicted in Fig. 7. The Ta/CoFeB/MgO trilayer is patterned into a 30 μm × 30 μm square with two contact pads. A long conducting strip consists of Ta (5 nm)/Cu (200 nm)/Au (50 nm) is fabricated in parallel with the sample for field calibration purpose. The width of the strip *w* is 30 μm, and the distance *d* between the strip and sample is 100 μm. We apply the linearly polarized light at the center of the sample film and a sinusoidal in-plane AC current at 1013 Hz either in the sample (1 mA) or in the conducting strip (100 mA). The Kerr rotation of the polarization due to the magnetization reorientation is analyzed by using the optical bridge apparatus that was reported in our previous work [36].

In the $H // I$ configuration, the relation between current induced SOT fields and the modulation of magnetization has been shown in Eqs. (9) and (10). Since we used normal incident light with 45° linear polarization with respect to the *x*-axis, the signal only depends on the polar angle as

$$\Delta V \propto \alpha_{polar} \sin\theta_0 \Delta\theta \quad (18)$$

Therefore, we derive the polar MOKE response from Eqs. (9) and (18) as

$$\Delta V \propto \alpha_{polar} \frac{\sin\theta_0 H_t}{H_P \cos 2\theta_0 + H \sin\theta_0} \quad (19)$$

The signal is calibrated with a known field by passing the current through the calibration wire. An out-of-plane magnetic field is generated on the sample that is analogous to the effect of SOT fields. The magnitude of the calibration field is given by $H_{ca} = \frac{I}{2\pi d}$. A 100 mA AC current generates 1.53 ± 0.13 Oe magnetic field, where the error is due to the finite width of the calibration strip. The polar MOKE response with current in the calibration wire is written as

$$\Delta V_{cal} \propto \alpha_{polar} \frac{\sin^2\theta_0 H_{cal}}{H_P \cos 2\theta_0 + H \sin\theta_0} \quad (20)$$

Comparing Eq. (19) and (20), we obtain the damping-like SOT effective field as

$$H_t = \frac{\Delta V}{\Delta V_{cal}} H_{cal} \sin\theta_0 \quad (21)$$

With the same derivation process, we obtain the formula in the $H \perp I$ configuration to calculate the field-like SOT effective field H_f as

$$H_f = \frac{\Delta V}{\Delta V_{cal}} H_{cal} \tan\theta_0 \quad (22)$$

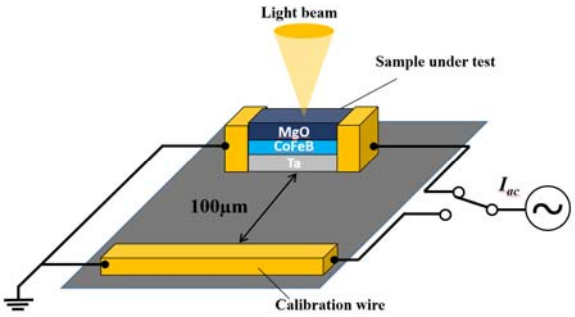

FIG.7. Sketch of the SOT measurement with MOKE technique

In each situation, we first apply current through the sample to detect the MOKE response ΔV induced by SOT effective fields. Then, we apply the current in the calibration wire to measure the calibration signal ΔV_{cal}. From the DC MOKE, we determine the equilibrium angle θ_0 at each magnetic field. Fig. 8a and 8b show the plots of the polar MOKE signals corresponding to the SOTs (black curve) and the calibration field (red curve) as a function of the external magnetic field in the two configurations. In the $H // I$ configuration, the MOKE single only depends on damping-like SOT field $\vec{H}_t = -b\vec{\sigma} \times \vec{M} / \gamma$. Therefore, we can see from Fig. 8a that the data due to SOTs changes its sign with the magnetic field. On the other hand, the field-like SOT field $\vec{H}_f = -a\vec{\sigma} / \gamma$ is a constant. Therefore, the curves corresponding to field-like SOT field in the $H \perp I$ configuration are symmetric with respect to the external magnetic field. We calculate the H_t and H_f from Eq. (21) and Eq. (22) respectively. Because the MOKE technique with calibration field does not require the fitting of the measurement curve, the measurement scheme we developed here is more accurate in determining the angular dependence of SOTs than the harmonic Hall technique. The SOT coefficient H_t / j_{Ta} and H_f / j_{Ta} are plotted versus polar angle in Fig. 8b and 8d, respectively. The ratio of H_f / H_t is around eight in this study on PMA films, suggesting a strong Rashba effect. The ratio in Pt/CoFeB bilayer [36] with in-plane anisotropy is much smaller where the SOTs are mostly attributed to SHE. Both damping-like and field-like SOTs show non-trivial significant angular dependence. The SOTs are maximum

near $\theta_0 = 90°$. The simple theoretical calculation based on 2D free-electron model with Rashba spin-orbit coupling also predicted the similar trend in the angular dependence [48]. Based on the non-trivial angular dependence and magnitude of SOTs, we believe the Rashba effect is the predominant mechanism in Ta/CoFeB/MgO trilayer structures. However, there are discrepancies between experimental results and theoretical predictions. In the 20-30 angle region, the SOTs is not monotonically increasing with the polar angle of magnetization. In addition, the magnitude and the increasing rate of SOTs after 60 degree are not reproduced in the theoretical modeling. Our results suggest that the current theoretical model is not sufficient to describe the entire angular dependence of SOTs in this system.

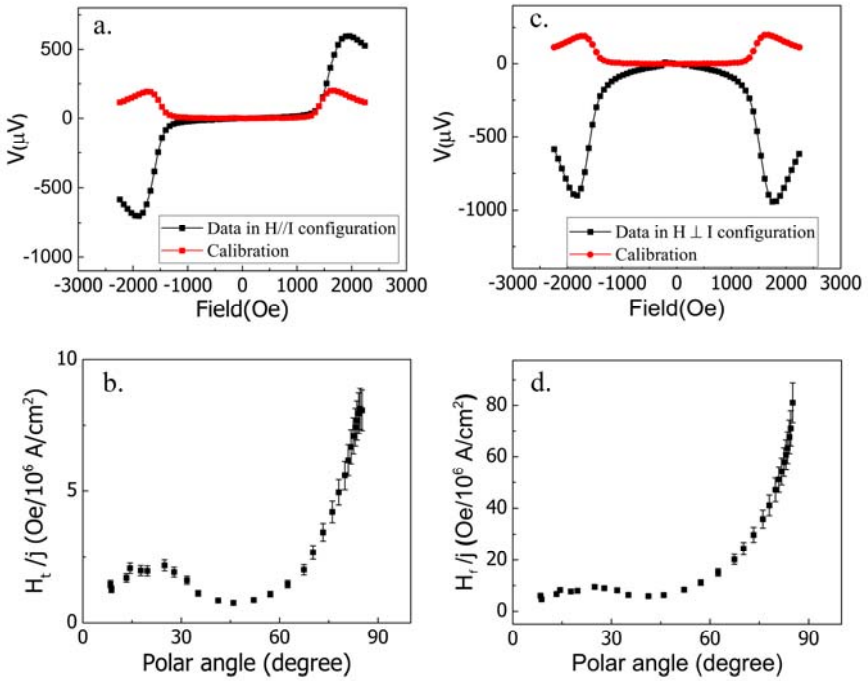

FIG.8. The MOKE response with 1 mA current (1.1×10^6 A/cm^2 current density in Ta) applied in the sample (black) and 1.53 Oe calibration field (red) under the configurations of (a) $H // I$ and (c) $H \perp I$. The calculated coefficient of damping-like torque (b) and field-like torque (d) as a function of the magnetization angle.

V. Conclusion

In summary, we have performed second harmonic Hall and MOKE measurements on Ta/CoFeB/MgO trilayers in order to quantify SOTs. We have also derived an algorithm to extract the angle dependence of SOTs. The second harmonic Hall measurements are widely employed to quantify SOTs. We have shown that this technique is sensitive to the fitting parameters. A small change in the fitting parameter leads to a significant error in the determination of SOTs in the medium polar-angle region. With MOKE technique, we eliminate the fitting procedure by implementing a field calibration to accurately measure the SOTs. The field-like torque has a larger magnitude than the damping-like torque. Both damping-like and field-like torques reach the maximum when the magnetization lies in the film plane, as expected from the theoretical model with interfacial Rashba spin-orbit interaction. However, the measured SOTs show a complex dependence on the polar angle of magnetization. It requires further theoretical efforts to fully understand the mechanism of SOTs. The accurate angle dependence of SOTs is also valuable to the study of magnetic dynamics induced by SOTs. The experiments on the layer thickness will be necessary to complete the study, which requires the quantification of the conductivity and other interfacial effects [49] at the ultrathin region.

Acknowledgment: The work is supported by NSF grant DMR-1505192 and the Center for NanoFerroic Devices (CNFD) under the Nanoelectronics Research Initiative (NRI).

[1] L. Liu, C.-F. Pai, Y. Li, H. Tseng, D. Ralph, and R. Buhrman, Science **336**, 555 (2012).

[2] X. Fan, J. Wu, Y. Chen, M. J. Jerry, H. Zhang, and J. Q. Xiao, Nature communications **4**, 1799 (2013).

[3] G. Yu, P. Upadhyaya, Y. Fan, J. G. Alzate, W. Jiang, K. L. Wong, S. Takei, S. A. Bender, L.-T. Chang, and Y. Jiang, Nature nanotechnology **9**, 548 (2014).

[4] X. Zhang, C. H. Wan, Z. H. Yuan, Q. T. Zhang, H. Wu, L. Huang, W. J. Kong, C. Fang, U. Khan, and X. F. Han, Physical Review B 94, 174434 (2016).

[5] C. Zhang, S. Fukami, H. Sato, F. Matsukura, and H. Ohno, Applied Physics Letters **107**, 012401 (2015).

[6] I. M. Miron, K. Garello, G. Gaudin, P.-J. Zermatten, M. V. Costache, S. Auffret, S. Bandiera, B. Rodmacq, A. Schuhl, and P. Gambardella, Nature **476**, 189 (2011).

[7] S. I. Kiselev, J. Sankey, I. Krivorotov, N. Emley, R. Schoelkopf, R. Buhrman, and D. Ralph, Nature **425**, 380 (2003).

[8] L. Liu, C.-F. Pai, D. Ralph, and R. Buhrman, Physical Review Letters **109**, 186602 (2012).

[9] L. Liu, T. Moriyama, D. Ralph, and R. Buhrman, Physical Review Letters **106**, 036601 (2011).

[10] V. E. Demidov, S. Urazhdin, H. Ulrichs, V. Tiberkevich, A. Slavin, D. Baither, G. Schmitz, and S. O. Demokritov, Nature Materials **11**, 1028 (2012).

[11] Z. Duan, A. Smith, L. Yang, B. Youngblood, J. Lindner, V. E. Demidov, S. O. Demokritov, and I. N. Krivorotov, Nature Communications **5** (2014).

[12] K.-S. Ryu, L. Thomas, S.-H. Yang, and S. Parkin, Nature Nanotechnology **8**, 527 (2013).

[13] P. Haazen, E. Murè, J. Franken, R. Lavrijsen, H. Swagten, and B. Koopmans, Nature Materials **12**, 299 (2013).

[14] I. M. Miron, T. Moore, H. Szambolics, L. D. Buda-Prejbeanu, S. Auffret, B. Rodmacq, S. Pizzini, J. Vogel, M. Bonfim, and A. Schuhl, Nature Materials **10**, 419 (2011).

[15] W. Jiang, P. Upadhyaya, W. Zhang, G. Yu, M. B. Jungfleisch, F. Y. Fradin, J. E. Pearson, Y. Tserkovnyak, K. L. Wang, O. Heinonen, S. G. E. te Velthuis, and A. Hoffmann, Science **349**, 283 (2015).

[16] G. Yu, P. Upadhyaya, X. Li, W. Li, S. K. Kim, Y. Fan, K. L. Wong, Y. Tserkovnyak, P. K. Amiri, and K. L. Wang, Nano Letters **16**, 1981 (2016).

[17] M. Stiles and A. Zangwill, Physical Review B **66**, 014407 (2002).

[18] I. Mihai Miron, G. Gaudin, S. Auffret, B. Rodmacq, A. Schuhl, S. Pizzini, J. Vogel, and P. Gambardella, Nature Materials **9**, 230 (2010).

[19] M. Zimmler, B. Özyilmaz, W. Chen, A. Kent, J. Sun, M. Rooks, and R. Koch, Physical Review B **70**, 184438 (2004).

[20] J. C. Sankey, Y.-T. Cui, J. Z. Sun, J. C. Slonczewski, R. A. Buhrman, and D. C. Ralph, Nature Physics **4**, 67 (2008).

[21] J. Slonczewski, Journal of Magnetism and Magnetic Materials **247**, 324 (2002).

[22] S. Zhang, P. Levy, and A. Fert, Physical Review Letters **88**, 236601 (2002).

[23] J. Hirsch, Physical Review Letters **83**, 1834 (1999).

[24] C.-F. Pai, L. Liu, Y. Li, H. Tseng, D. Ralph, and R. Buhrman, Applied Physics Letters **101**, 122404 (2012).

[25] A. R. Mellnik, J. S. Lee, A. Richardella, J. L. Grab, P. J. Mintun, M. H. Fischer, A. Vaezi, A. Manchon, E. A. Kim, N. Samarth, and D. C. Ralph, Nature **511**, 449 (2014).

[26] A. Vedyayev, N. Strelkov, M. Chshiev, N. Ryzhanova, and B. Dieny, arXiv preprint arXiv:1108.2589 (2011).

[27] P. M. Haney, H.-W. Lee, K.-J. Lee, A. Manchon, and M. D. Stiles, Physical Review B **87**, 174411 (2013).

[28] D. Pesin and A. MacDonald, Physical Review B **86**, 014416 (2012).

[29] X. Wang and A. Manchon, Physical Review Letters **108**, 117201 (2012).

[30] A. Manchon and S. Zhang, Physical Review B **78**, 212405 (2008).

[31] U. H. Pi, K. W. Kim, J. Y. Bae, S. C. Lee, Y. J. Cho, K. S. Kim, and S. Seo, Applied Physics Letters **97**, 162507 (2010).

[32] T. Suzuki, S. Fukami, N. Ishiwata, M. Yamanouchi, S. Ikeda, N. Kasai, and H. Ohno, Applied Physics Letters **98**, 142505 (2011).

[33] F. Freimuth, S. Blügel, and Y. Mokrousov, Physical Review B **90**, 174423 (2014).

[34] V. Amin and M. Stiles, arXiv preprint arXiv:1604.06502 (2016).

[35] A. Manchon, arXiv preprint arXiv:1204.4869 (2012).

[36] X. Fan, H. Celik, J. Wu, C. Ni, K.-J. Lee, V. O. Lorenz, and J. Q. Xiao, Nature Communications **5** (2014).

[37] S. Ikeda, K. Miura, H. Yamamoto, K. Mizunuma, H. Gan, M. Endo, S. Kanai, J. Hayakawa, F. Matsukura, and H. Ohno, Nature materials **9**, 721 (2010).

[38] W.-G. Wang, M. Li, S. Hageman, and C. Chien, Nature materials **11**, 64 (2012).

[39] S. Kanai, M. Yamanouchi, S. Ikeda, Y. Nakatani, F. Matsukura, and H. Ohno, Applied Physics Letters **101**, 122403 (2012).

[40] W.-G. Wang, S. Hageman, M. Li, S. Huang, X. Kou, X. Fan, J. Q. Xiao, and C. Chien, Applied Physics Letters **99**, 102502 (2011).

[41] H. Yang, M. Chshiev, B. Dieny, J. Lee, A. Manchon, and K. Shin, Physical Review B **84**, 054401 (2011).

[42] S. Peng, M. Wang, H. Yang, L. Zeng, J. Nan, J. Zhou, Y. Zhang, A. Hallal, M. Chshiev, and K. L. Wang, Scientific reports **5** (2015).

[43] C. Zhang, M. Yamanouchi, H. Sato, S. Fukami, S. Ikeda, F. Matsukura, and H. Ohno, Applied Physics Letters **103**, 262407 (2013).

[44] J. Kim, J. Sinha, M. Hayashi, M. Yamanouchi, S. Fukami, T. Suzuki, S. Mitani, and H. Ohno, Nature materials **12**, 240 (2013).

[45] X. Qiu, P. Deorani, K. Narayanapillai, K.-S. Lee, K.-J. Lee, H.-W. Lee, and H. Yang, Scientific Reports **4**, 4491 (2014).

[46] K. Garello, I. M. Miron, C. O. Avci, F. Freimuth, Y. Mokrousov, S. Blügel, S. Auffret, O. Boulle, G.

Gaudin, and P. Gambardella, Nature nanotechnology **8**, 587 (2013).
[47] C. O. Avci, K. Garello, C. Nistor, S. Godey, B. Ballesteros, A. Mugarza, A. Barla, M. Valvidares, E. Pellegrin, and A. Ghosh, Physical Review B **89**, 214419 (2014).
[48] G. Allen, S. Manipatruni, D. E. Nikonov, M. Doczy, and I. A. Young, Physical Review B **91**, 144412 (2015).
[49] S. Emori, T. Nan, A. M. Belkessam, X. Wang, A. D. Matyushov, C. J. Babroski, Y. Gao, H. Lin, and N. X. Sun, Physical Review B **93**, 180402 (2016).
[50] K.-S. Lee, D. Go, A. Manchon, P. M. Haney, M. D. Stiles, H.-W. Lee, and K.-J. Lee, Physical Review B **91**, 144401 (2015).
[51] M. Hayashi, J. Kim, M. Yamanouchi, and H. Ohno, Physical Review B **89**, 144425 (2014).
[52] X. Fan, A. R. Mellnik, W. Wang, N. Reynolds, T. Wang, H. Celik, V. O. Lorenz, D. C. Rlaph, and J. Q. Xiao, arXiv preprint arXiv:1509.01266 (2015)